

Accepted Manuscript

Fabrication of ZnO, ZnS, Ag-ZnS, and Au-ZnS microspheres for photocatalytic activities, CO oxidation and 2-hydroxyterephthalic acid synthesis

Young In Choi, Seungwon Lee, Seog K. Kim, Young-II Kim, Dae Won Cho, Mohammad Mansoob Khan, Youngku Sohn



PII: S0925-8388(16)30639-9

DOI: [10.1016/j.jallcom.2016.03.070](https://doi.org/10.1016/j.jallcom.2016.03.070)

Reference: JALCOM 36958

To appear in: *Journal of Alloys and Compounds*

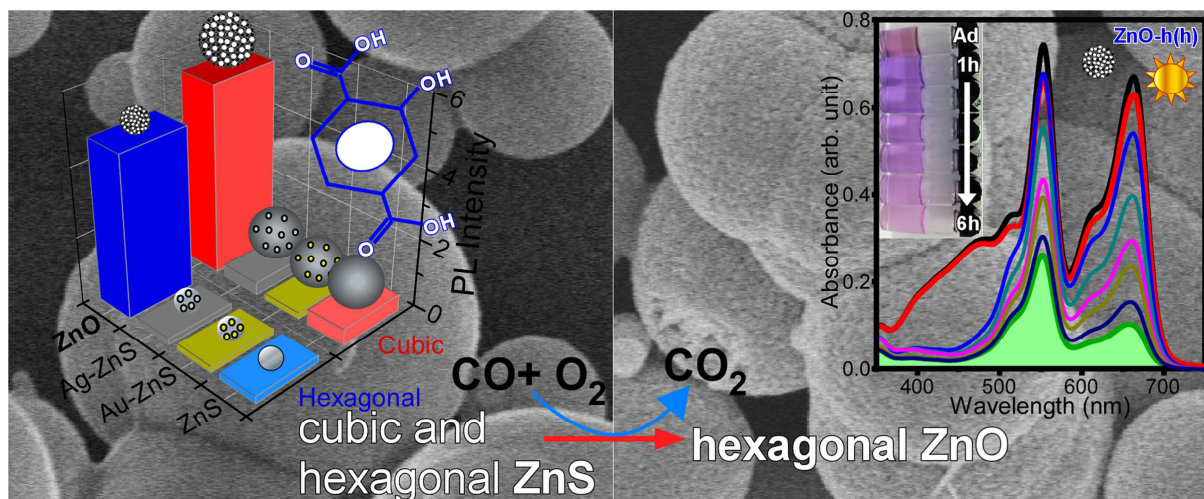
Received Date: 4 January 2016

Revised Date: 21 February 2016

Accepted Date: 11 March 2016

Please cite this article as: Y.I. Choi, S. Lee, S.K. Kim, Y.-I. Kim, D.W. Cho, M.M. Khan, Y. Sohn, Fabrication of ZnO, ZnS, Ag-ZnS, and Au-ZnS microspheres for photocatalytic activities, CO oxidation and 2-hydroxyterephthalic acid synthesis, *Journal of Alloys and Compounds* (2016), doi: 10.1016/j.jallcom.2016.03.070.

This is a PDF file of an unedited manuscript that has been accepted for publication. As a service to our customers we are providing this early version of the manuscript. The manuscript will undergo copyediting, typesetting, and review of the resulting proof before it is published in its final form. Please note that during the production process errors may be discovered which could affect the content, and all legal disclaimers that apply to the journal pertain.



Fabrication of ZnO, ZnS, Ag-ZnS, and Au-ZnS microspheres for photocatalytic activities, CO oxidation and 2-hydroxyterephthalic acid synthesis

Young In Choi,^{1,†} Seungwon Lee,^{1,†} Seog K. Kim,¹ Young-II Kim,¹ Dae Won Cho,¹
Mohammad Mansoob Khan,^{2,*} and Youngku Sohn^{1,*}

¹*Department of Chemistry, Yeungnam University, Gyeongsan 38541, Republic of Korea.*

²*Chemical Sciences, Faculty of Science, Universiti Brunei Darussalam, Jalan Tungku Link, Gadong, BE 1410, Brunei Darussalam.*

[†]These authors equally contributed to this work.

*Corresponding authors e-mail: youngkusohn@ynu.ac.kr; mmansoobkhan@yahoo.com

Abstract

This paper reports the synthesis of ZnS microspheres with cubic and hexagonal crystal phases using a solvothermal method. These materials were characterized by a range of techniques. The effects of Au and Ag-doping on ZnS were also examined. Hexagonal phase ZnO microspheres could be obtained by a CO oxidation process over the ZnS microspheres. The onset of CO oxidation occurred above 350°C, which was increased by Au and Ag doping. The synthesized materials were used for the photocatalytic degradation of mixed dyes {methylene blue (MB) + methyl orange (MO) + rhodamine B (RhB)}. The observed photocatalytic degradation rate over the photocatalysts was in the order, RhB < MB << MO. The photocatalytic degradation activity of the synthesized materials was observed in the order, Au-ZnS ≈ Ag-ZnS << ZnS < ZnO. ZnO was ~6 times more efficient in the photocatalytic synthesis of 2-hydroxyterephthalic acid than the ZnS and metal-doped ZnS. These results further support the importance and wide applications of the synthesized ZnS, Ag-ZnS, Au-ZnS and ZnO microspheres.

Key words: ZnO; ZnS; cubic and hexagonal; CO oxidation; photocatalytic dye degradation; 2-hydroxyterephthalic acid

1. Introduction

Metal oxides, such as TiO_2 , ZnO , SnO_2 and CeO_2 , are well known semiconductors for novel applications [1-4]. Among these, ZnO is one of the most studied metal oxide materials for catalysis, photocatalysis, photoelectrochemical, sensors, solar cells, and biological applications [1-20]. ZnO nanostructures are prepared by hydrothermal, solvothermal, electrodeposition, and chemical as well as physical deposition methods [1-20]. ZnO has a wide direct band gap (~ 3.37 eV), which restricts its activity to the UV region. In addition, a large exciton binding energy of 60 meV (or longer-lived electron-hole pair) limits the photodegradation reaction under normal conditions [12,14]. ZnS is a type of semiconductor (chalcogenides) that is also well known for its photocatalytic applications [21-34].

The advances in hybrid photoactive materials (metal-semiconductor) have resulted in significant progress in heterogeneous visible light-induced photocatalysis by suppressing the recombination of photogenerated electron-hole pairs. The catalytic and photocatalytic activities of ZnO and ZnS can be enhanced by hybridization with noble metals, such as silver (Ag) and gold (Au). Metals anchored/loaded to ZnO and ZnS nanocomposites have been prepared using a range of approaches [5-14,21-41], such as biogenic synthesis using biofilms [14], flame spray pyrolysis [36], photo-reduction/chemical reduction [37], and ball-milling [41]. Ansari et al. synthesized Ag- ZnO nanocomposites by an electrochemical biogenic synthesis method using an active biofilm electrode, and observed enhanced photocatalytic properties for the degradation of methyl orange, methylene blue and 4-nitrophenol [14]. Manna et al. prepared Ag@ ZnO -coated cotton fabrics by polyamine-mediated mineralization and a reduction method and revealed their photocatalytic activities for the photodegradation of rhodamine B (RhB) and the disinfection of bacteria under visible light [25]. Misra et al. prepared Au@ ZnS core-shell nanoparticles and reported an increase in photocatalytic activity for methyl orange and an increase in photocurrent induced by surface plasmon resonance [25]. Photocatalytic CO_2 reduction was also tested over Ru-functionalized ZnS , and CO_2 was found to be major reduction product [26]. Zhang et al. decorated ZnO nanorods with Ag nanoprisms and Ag nanoparticles, and observed that Ag nanoprisms produced a much higher photocurrent intensity owing to the shape-dependent localized surface plasmon

resonance (SPR) effect [35]. The SPR of Ag (or Au) is believed to enhance visible light harvesting and increase the photocatalytic activity [14,35,36,38]. In addition, the band gap and defects play important roles in the photocatalytic activity of a material [1-4,14,39]. Oxygen vacancies formed by impurity doping are also known to play a significant role in improving the photocatalytic activity [1-4,18]. Fang et al. controlled the surface defects of ZnO nanorods by varying the quenching temperature and cooling rate. The concentration of defects was found to be responsible for suppression electron-hole recombination and increasing the photocatalytic dye degradation rates [18].

This paper reports a very simple and facile method for the synthesis of cubic and hexagonal ZnS, Ag-ZnS and Au-ZnS microspheres using a solvothermal method. Hexagonal phase ZnO microspheres were synthesized using a unique CO oxidation treatment. Most studies reported an improvement in the photocatalytic activity upon testing with a pure dye at the optimal amount of Ag on ZnO. The photocatalytic activity also depends on the nature of the dye and reaction conditions. In this study, a more complicated mixed dye {methyl orange (MO) + methylene blue (MB) + RhB} was used as a model system. The photocatalytic dye degradation rate was expected to be different because the three different dyes will show various UV-visible absorption bands and different surface charges. To the best of the authors' knowledge, this is the first report of the synthesis of novel photocatalysts and the treatment of mixed dyes using ZnS, Ag-ZnS, Au-ZnS, and ZnO microspheres, on CO oxidation, and the visible light-assisted synthesis of 2-hydroxyterephthalic acid. The syntheses of ZnO microspheres and 2-hydroxyterephthalic acid are the exceptional findings of this study, which is efficient and facile.

2. Experimental Section

2.1. Chemicals

Zn(NO₃)₂·6H₂O (98%), ZnSO₄·7H₂O (≥ 99.0%), Au(III) chloride trihydrate (99.9%), and thiourea (≥99.0%) were purchased from Sigma-Aldrich. Ethylene glycol (EG, 99%, Daejung Co., South Korea), AgNO₃ (Duksan Co., South Korea), MO (TCI, Japan), MB

(Merck, Germany), RhB (Junsei Chem., Japan), and terephthalic acid (TCI, Japan) were used as received.

2.2. ZnS synthesis, and Au and Ag-loading

ZnS with two different crystal phases were synthesized using a solvothermal method as described below. The two different ZnS nanostructures were designated ZnS(h) and ZnS(c). For the synthesis of ZnS(h), solutions of 0.1 M zinc nitrate and 0.1 M thiourea in ethylene glycol (EG) were prepared. 20.0 mL of the two solutions were mixed thoroughly, transferred to a Teflon-lined stainless autoclave and placed in an oven at 200°C for 12 hrs. After the reaction, the final product was naturally cooled, collected by centrifugation, and washed several times with deionized water and ethanol. The white powder was finally dried in an oven at 80°C. For the synthesis of ZnS(c), solutions of 0.1 M zinc sulfate and 0.1 M thiourea were prepared in EG. A 20.0 mL volume of each of the two solutions were mixed and the same experimental procedures used for ZnS(h) were followed. For Au and Ag doping, 1.0 mol% of a 0.1 M Au chloride solution or 0.1 M Ag nitrate solution were mixed with the abovementioned solutions before being placed in an oven. For Au and Ag-doped ZnS(h) and ZnS(c) samples, the samples were designated as Au-ZnS(h), Ag-ZnS(h), Au-ZnS(c), and Ag-ZnS(c) microspheres.

2.3. Photocatalysts characterization

To examine the crystal structures of the synthesized powder materials, powder X-ray diffraction (XRD, PANalytical X'Pert Pro MPD) was performed using Cu K α radiation (40 kV and 30 mA). The morphologies were examined by field-emission scanning electron microscopy (FE-SEM, Hitachi SE-4800) and transmission electron microscopy (TEM, Hitachi H-7600) operated at 100 kV. For the SEM and TEM observations, the samples were mounted on a Si substrate and a lacey carbon Cu grid, respectively. A double beam UV-Vis spectrophotometer (SCINCO NeoSys-2000) was used to measure the UV-Vis diffuse reflectance/absorption spectra of the powdered samples. The photoluminescence (PL, SCINCO FluoroMate FS-2) spectra of the powder samples were

obtained at an excitation wavelength of 250 nm. X-ray photoelectron spectroscopy (XPS, Thermo-VG Scientific K-Alpha) was performed using a monochromated Al $K\alpha$ X-ray source (1486.6 eV) and a hemispherical energy analyzer. An electron flood gun was used to neutralize the surface charge. For the Brunauer-Emmett-Teller (BET) surface area measurements, a ChemBET TPR/TPD analyzer (Quantachrome Instruments, USA) equipped with a thermal conductivity detector was used. Before the BET measurements, the samples were degassed at 200°C for 2 hrs.

2.4. CO oxidation and ZnO preparation

ZnS conversion to ZnO was performed by a CO oxidation reaction over the ZnS samples. The CO oxidation experiment was conducted under CO(1.0%)/O₂(2.5%)/N₂ mixed gas flow conditions. The gas flow rate and heating rate were fixed at 40 mL/min and 10 K/min, respectively. The powder sample (10 mg) was mounted in a U-shape quartz tube (an inner diameter of 4.0 mm). The reaction product was monitored using a quadrupole mass spectrometer (RGA200, Stanford Research System, USA). The CO conversion percentage (%) was calculated using $\{([\text{CO}]_{\text{in}} - [\text{CO}]_{\text{out}}) / [\text{CO}]_{\text{in}} \times 100\}$.

2.5. Adsorption and photocatalytic dye degradation tests

To prepare the mixed dye solution, the same amounts of methyl orange (MO), rhodamine B (RhB) and methylene blue (MB) solutions was mixed to have the same concentration of 10 mg/L. For the adsorption (in dark) and photocatalytic dye degradation tests (under visible light), 10 mg of the photocatalyst was dispersed fully into a 50 mL mixed dye solution and stirred in the dark. Upon achieving the adsorption-desorption equilibrium, the mixed dye solution and photocatalyst mixture was irradiated with visible light with magnetic stirring. The photodegradation experiment was observed for 6 hrs and the rate of dye photodegradation was monitored by taking 2.0 mL of the sample every 1 hr, centrifuging it to remove the catalyst and recording the UV-vis spectrum. The dye concentrations after adsorption and visible light irradiation (with time)

were obtained by measuring the level of UV-visible absorption using a UV-Vis spectrophotometer (Jasco V-530).

2.6. Synthesis of 2-hydroxyterephthalic acid

The synthesis of 2-hydroxyterephthalic acid (HTPA) was performed to examine the formation of $\cdot\text{OH}$ radicals over the photocatalyst in a solution during visible light irradiation. The photocatalyst was dispersed in 50 mL of a 0.002 M NaOH (with 2.4×10^{-5} mol terephthalic acid) solution. After irradiating visible light for 6 hrs, the solution was centrifuged and the photoluminescence (PL) spectrum was measured. HTPA was formed by a reaction of terephthalic acid (TPA) with $\cdot\text{OH}$ radicals. The amount of HTPA could be examined by PL because TPA is non-luminescent, whereas HTPA is. The PL measurements were conducted at an excitation wavelength of 320 nm using a SCINCO FluoroMate FS-2.

3. Results and Discussion

3.1. Morphology and XRD of ZnS and Au and Ag-doped ZnS

Figure 1 shows SEM images and XRD patterns of the as-synthesized ZnS(h), ZnS(c), and Ag and Au-doped ZnS(h) and ZnS(c) microspheres. All SEM images show spherical shapes but different sizes. The diameters of the ZnS(h) microspheres prepared with $\text{Zn}(\text{NO}_3)_2$ and thiourea in EG were 200-300 nm. The diameters of the Ag-doped ZnS(h) increased to 300-500 nm. For Au-doped ZnS(h), the diameters were increased further to 800-1000 nm. The diameters of the ZnS(c) sample prepared with ZnSO_4 and thiourea in EG were ~10 times larger than that of ZnS(h) and was found to be 1 - 3 μm . For the Ag-doped ZnS(c) sample, the particle size was much smaller. On the other hand, for Au-doped ZnS(c), larger particles were also observed, compared to undoped ZnS(c).

The XRD patterns of ZnS(h) and ZnS(c) revealed two different sizes. Interestingly, both the XRD patterns were entirely different. For ZnS(h), the XRD peaks were well matched to the reference patterns of wurtzite hexagonal (P63mc) ZnS (JCPDS 1-080-

0007) [33]. On the other hand, for ZnS(c), the XRD patterns appeared to match the reference patterns of cubic (F-43m) ZnS (JCPDS 1-080-0020). All crystal planes were assigned to the corresponding XRD peaks. Upon Ag-doping to ZnS(h), the XRD patterns became sharper, particularly for the (002), (110) and (112) planes. For the Ag-doped ZnS(c), the (111), (220) and (311) planes became sharper. No XRD peaks for Ag were found, indicating the amorphous nature and/or small amount of Ag. Upon Au-doping of ZnS(h) and ZnS(c), the XRD patterns of hexagonal ZnS(h) and cubic ZnS(c) showed no significant change. On the other hand, for the Au-doped samples, new XRD peaks were observed at $2\theta = 38.2^\circ$, 44.3° , 64.6° , and 77.5° , which were assigned to the (111), (002), (022), and (113) planes, respectively, of cubic crystal phase (Fm-3m, JCPDS 98-004-4362) Au. The Au XRD peaks of Au-ZnS(c) were more intense than those of Au-ZnS(h). This confirms the synthesis of ZnS(h), ZnS(c), Ag-ZnS(h), Ag-ZnS(c), Au-ZnS(h), and Au-ZnS(c) microspheres and their purity.

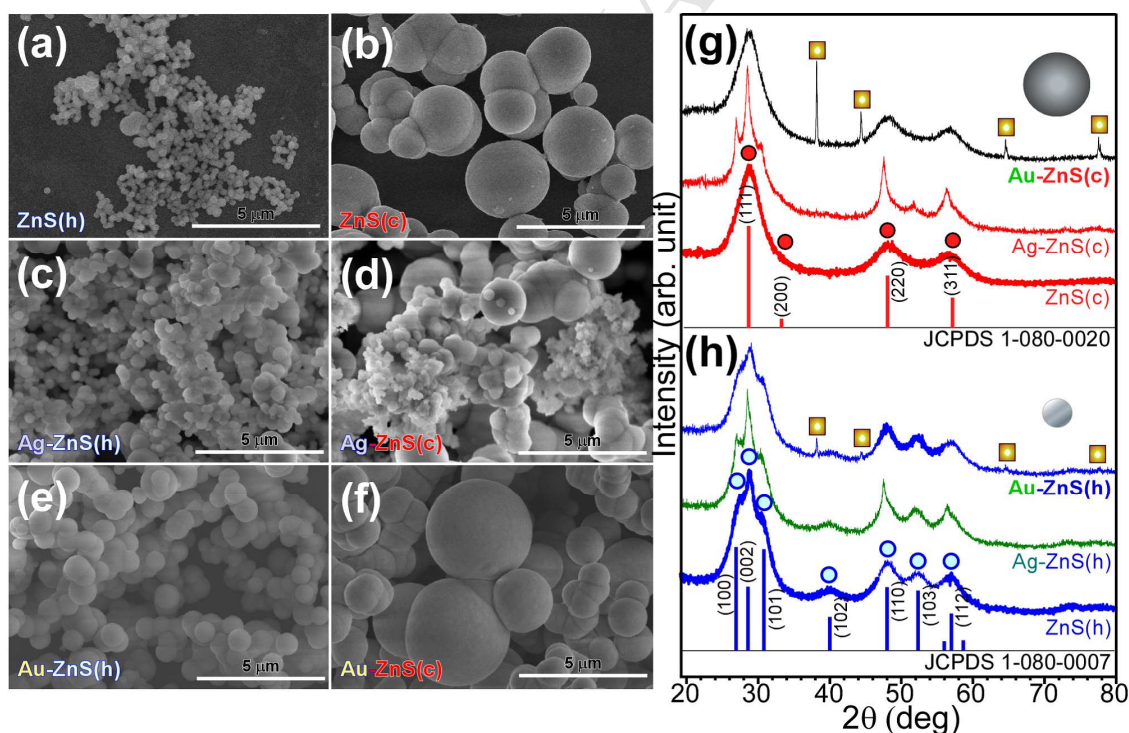


Figure 1. SEM images (left) of (a) ZnS(h), (b) ZnS(c), (c) Ag-ZnS(h), (d) Ag-ZnS(c), (e) Au-ZnS(h), and (f) Au-ZnS(c) samples, and the corresponding XRD profiles (g and h).

3.2. UV-Vis absorption and PL of ZnS and Au and Ag-doped ZnS

Figure 2 shows the UV-Vis diffuse reflectance absorption (Fig. 2a) and PL spectra (Fig. 2c and 2d) of ZnS(h), ZnS(c), Ag-ZnS(h), Ag-ZnS(c), Au-ZnS(h), and Au-ZnS(c) samples. The $[\alpha h\nu]^2$ vs. photon energy (E, eV) plots are also shown (Fig. 2b), where α and h are the absorbance and Planck's constant, respectively. The Tauc equation, $\alpha h\nu = A(h\nu - E_g)^{n/2}$, was used to estimate the band gap, where A is an empirical value and n is 4 for an indirect band gap (e.g., TiO₂) and $n = 1$ for a direct band gap (e.g., ZnS and ZnO) [42,43]. For undoped ZnS(h) and ZnS(c), the band gaps were estimated to be 3.6 and 3.45 eV, respectively, which is in good agreement with the literature [33]. Zeng et al. reported wurtzite ZnS films (band gaps of 3.50–3.64 eV) prepared by spray pyrolysis at 310°C using a solution of ZnCl₂ and thioacetamide [33]. For the Au and Ag-doped samples, the absorption in the visible region were strongly enhanced. On the other hand, for Au-doped ZnS(c), the band gap edge showed a slight change, compared to that of undoped ZnS(c). This was attributed to the quantum confinement effect and surface plasmon resonance effects of the synthesized materials [14,35,36,38].

The PL spectra (Fig. 2c) of ZnS(h) and ZnS(c) showed broad peaks near 380 nm and 470 nm, which were attributed to band gap emission and defects, respectively [33]. For the Au and Ag-doped samples (Fig. 2d), the PL peaks decreased significantly, which is due to a metal-dipole quenching effect [42,43]. For Au-ZnS(c), the PL intensity showed a small decrease compared to the other metal-doped samples. This was attributed to the decrease in charge carrier recombination [42-46].

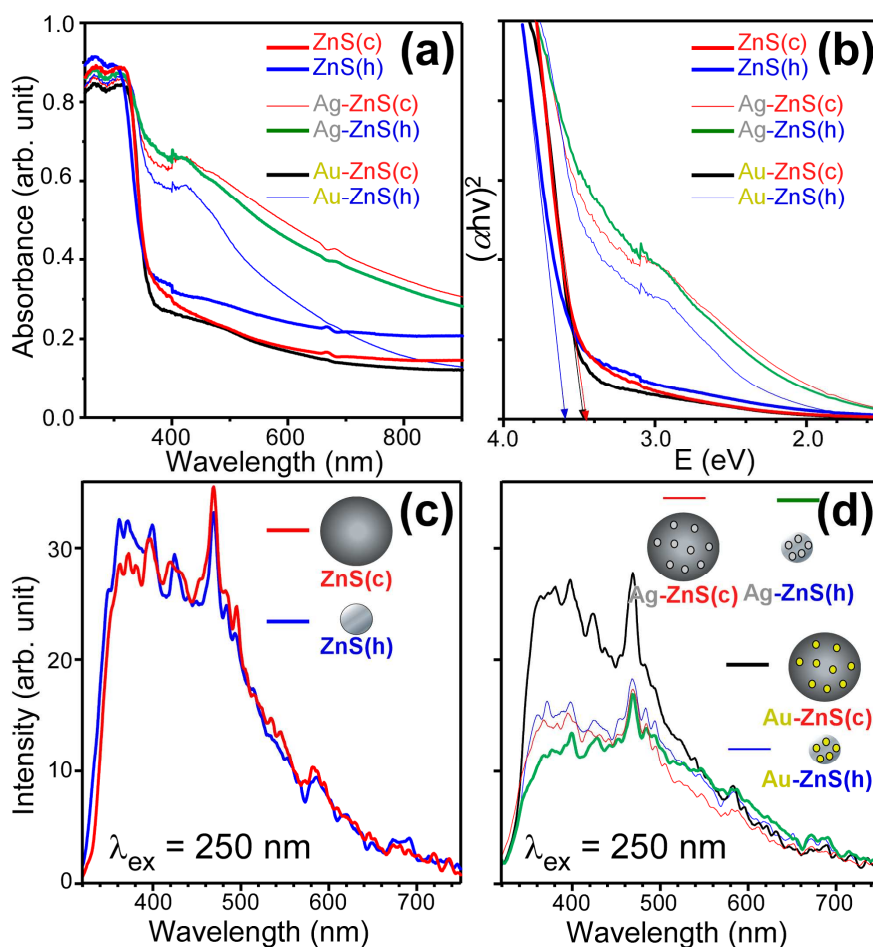


Figure 2. UV-visible diffuse reflectance absorption spectra (a, and b), and PL (c, and d) spectra of the ZnS(h), ZnS(c), Ag-ZnS(h), Ag-ZnS(c), Au-ZnS(h), and Au-ZnS(c) samples. An excitation wavelength of 250 nm was used to obtain the PL spectra.

3.3. XPS of cubic and hexagonal phase ZnS

XPS was used to examine the surface electronic structures of cubic and hexagonal phase ZnS. Figure 3 shows the survey and high resolution Zn 2p and O 1s XP spectra of hexagonal phase ZnS(h) and cubic phase ZnS(c). The survey scan only showed Zn and S, with C as a surface impurity. The high resolution Zn 2p peaks were normalized to the same intensity. The S 2p peaks were rescaled with the same normalization factor for Zn 2p. For ZnS(h), the Zn 2p_{3/2} (Zn 2p_{1/2}) XPS peak was observed at a binding energy (BE) of 1021.5 (1044.1) eV, with a spin-orbit splitting of 22.6 eV, which is in good agreement

with the literature [46-48]. For ZnS(c), the Zn 2p XPS peak was observed at a higher BE (by 0.5 eV) with the same spin-orbit splitting energy. The S 2p XPS peaks of ZnS(h) and ZnS(c) were observed at 161.6 and 161.9 eV, respectively. Interestingly, the S 2p XPS peak area for ZnS(h) was ~10% larger than that for ZnS(c). This indicates that the facets of ZnS(h) have more exposed S [46].

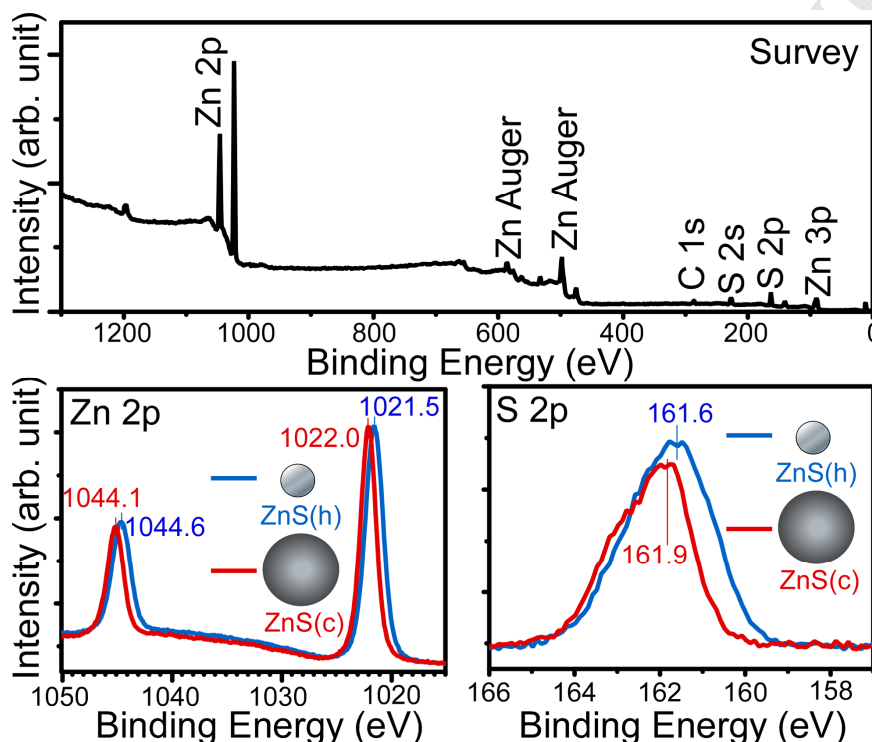


Figure 3. Survey and high resolution Zn 2p and O 1s XP spectra of hexagonal phase ZnS(h) and cubic phase ZnS(c).

3.4. Photocatalytic dye degradation over bare ZnS and Au and Ag-doped ZnS

The photocatalytic dye degradation of mixed dyes (MO + RhB + MB) was performed under visible light irradiation. First, adsorption-desorption was examined and the photocatalytic dye degradation of mixed dyes over ZnS(h), ZnS(c), Ag-ZnS(h), Ag-ZnS(c), Au-ZnS(h), and Au-ZnS(c) was then performed [41,49,50]. Each sample was dispersed in 50 mL of the mixed dye solution, which were a mixture of MO, RhB and MB with the same concentration of 10 mg/L. Figure 4 shows the UV-Vis absorption

spectra of each sample after adsorption in the dark and after photoirradiation. Because the mixed dye contains three different dyes, the corresponding absorption spectrum shows three absorption regions of MO (450 nm), RhB (550 nm) and MB (650 nm). The three peaks positions were used to analyze the extent of photocatalytic dye degradation. For ZnS(c), upon adsorption in the dark, the three UV-Vis absorption intensities decreased by less than 10% (or $C_{ad}/C_0 = 90\%$), where C_0 and C_{ad} are the UV-Vis absorption intensities before (initial) and after adsorption, respectively. Upon Ag and Au-doping of ZnS(c), the adsorption performance was decreased. The UV-Vis absorption intensities in the MO and RhB regions showed a negligible decrease, and that in the MB region showed only a 2-3% decrease. For ZnS(h), MO and RhB showed 12% adsorption, whereas MB showed only 2% adsorption over the photocatalyst. Upon Ag and Au-doping into ZnS(h), the adsorption performance for MO and RhB decreased, whereas that of MB increased. For the photocatalytic dye degradation over ZnS(c), the UV-Vis intensity was decreased gradually with increasing visible light irradiation. After 6 h, the UV-Vis absorption in the case of MO was decreased drastically. In the case of RhB, the UV-Vis absorption was decreased by 47% (or $C_{6h}/C_{ad} = 53\%$), where C_{6h} and C_{ad} are the UV-Vis absorption intensities after 6 h photoirradiation and adsorption, respectively. For MB, the UV-Vis absorption was decreased by 79% (or $C_{6h}/C_{ad} = 21\%$). The photocatalytic performance was observed in the order, RhB < MB << MO over ZnS(c). Upon Ag and Au-doping, the photocatalytic performance for RhB and MB decreased significantly but the performance for MO was unaffected. For Ag-doped ZnS(c), the RhB and MB absorption spectra decreased in intensity by 12% (or $C_{6h}/C_{ad} = 88\%$) and 51% (or $C_{6h}/C_{ad} = 49\%$), respectively. For Au-doped ZnS(c), the catalytic performance was somewhat better than the Ag-doped ZnS(c). The UV-Vis absorption spectra of RhB and MB were decreased by 17% (or $C_{6h}/C_{ad} = 83\%$) and 59% (or $C_{6h}/C_{ad} = 41\%$), respectively. For ZnS(h), the UV-Vis absorption spectra of RhB and MB were decreased by 47% (or $C_{6h}/C_{ad} = 53\%$) and 81% (or $C_{6h}/C_{ad} = 19\%$), respectively. Upon Ag and Au-doping, the catalytic activity also decreased. For Ag-ZnS(h), the UV-Vis absorption spectra of RhB and MB were decreased by 10% (or $C_{6h}/C_{ad} = 90\%$) and 62% (or $C_{6h}/C_{ad} = 48\%$), respectively. For Au-ZnS(h), the catalytic performance was somewhat poor compared to that for Ag-doped ZnS(h). The UV-Vis absorption spectra of RhB and MB showed decrease in intensity of

3% (or $C_{6h}/C_{ad} = 97\%$) and 44% (or $C_{6h}/C_{ad} = 56\%$), respectively. Although the absorption in the visible light was increased after Ag and Au-doping, the catalytic activity was poorer. This suggests that the photocatalytic mechanism is likely governed more by a dye-sensitized mechanism, which will be discussed below.

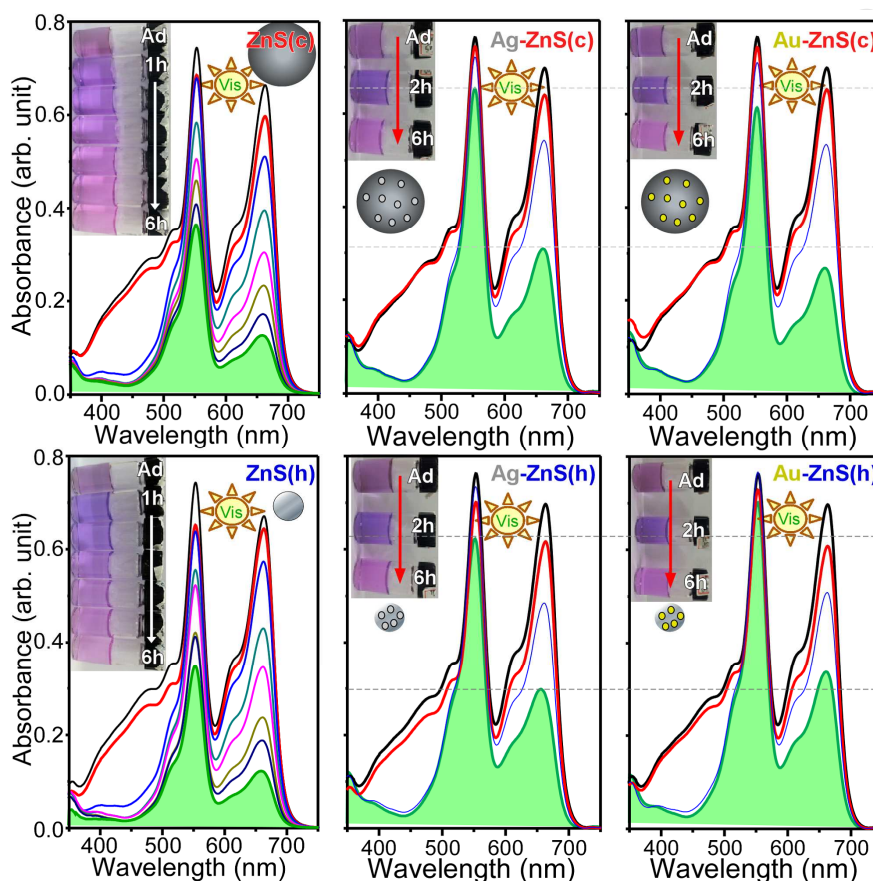


Figure 4. UV-Vis absorption spectra for the adsorption (C_{ad}/C_0) and photocatalytic dye degradation (C/C_{ad}) under visible light irradiation over bare (left column), Ag (middle column) and Au-doped (right column) cubic (top panel) and hexagonal (bottom panel) crystal phase ZnS microspheres.

3.5. CO oxidation of ZnS and Ag and Au-doped ZnS

The conversion of ZnS to ZnO is very important industrially. Figure 5 shows the first and second run CO oxidation profiles of ZnS(c), ZnS(h), Ag-ZnS(c), Ag-ZnS(h), Au-ZnS(c), and Au-ZnS(h) samples. The CO conversion % was calculated using

$\{([\text{CO}]_{\text{in}} - [\text{CO}]_{\text{out}}) / [\text{CO}]_{\text{in}} \times 100\%$ } [51-57]. For the first runs of the ZnS(c) and ZnS(h) microspheres, CO oxidation began to occur at approximately 370 and 350°C, respectively. In the second runs, the onset of CO oxidation was observed at 400 and 350°C, respectively. With increasing temperature, the CO oxidation conversion (%) in the second run was higher than that in the first run. The increase in CO conversion in the second run was attributed to the change in crystal phase [51,55] from ZnS to ZnO, as discussed below. For Ag and Au-doped ZnS(c), the CO oxidation profiles were similar. In addition, a difference in the onset of CO oxidation between the first and the second runs was also observed at a similar temperature of 420°C. The level of CO conversion increased sharply at the above temperature. For Ag and Au-doped ZnS(h), the CO oxidation profiles were somewhat different from those of the bare ZnS(c) and ZnS(h), and Ag and Au-doped ZnS(c). For the first runs of the Ag-ZnS(h) and Au-ZnS(h) microspheres, the CO oxidation onsets were observed at ~390 and 400°C, respectively. In the second runs, the CO oxidation onsets were observed at ~430 and 400°C, respectively. The Ag and Au-doped samples showed poor CO oxidation activity compared to the other samples.

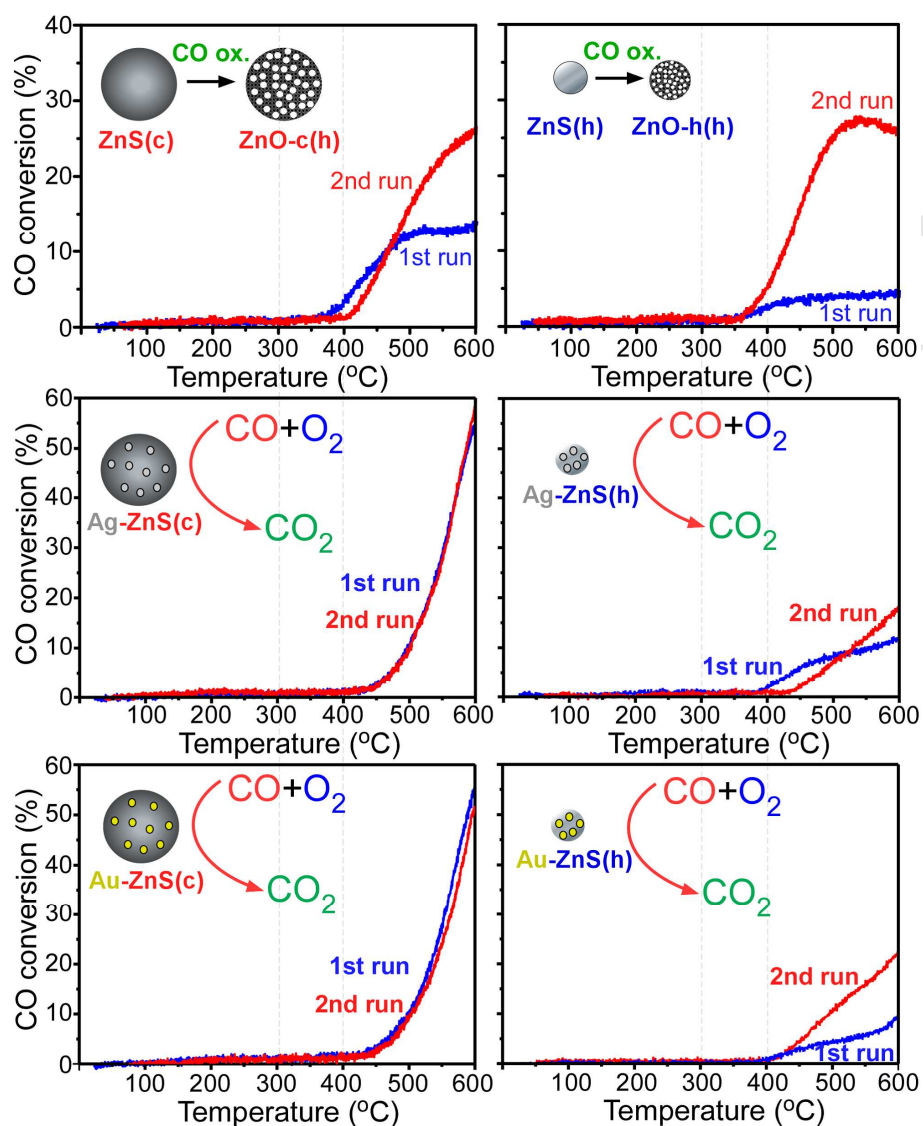


Figure 5. 1st and 2nd run CO oxidation profiles of the ZnS(c), ZnS(h), Ag-ZnS(c), Ag-ZnS(h), Au-ZnS(c), and Au-ZnS(h) samples.

3.6. Morphology and XRD of ZnO by CO oxidation of ZnS

The morphologies and XRD patterns of the ZnS(c) and ZnS(h) were examined after the CO oxidation reactions. Figure 6 shows SEM and TEM images and XRD patterns of the samples. The SEM and TEM images revealed microspheres with two different sizes; the samples from ZnS(h) and ZnS(c) were 200-300 nm and 1 - 3 μm in size, respectively. Although the sizes showed no critical changes after CO oxidation, the surface became

rough. TEM revealed the slight aggregation of smaller particles. Finally, the crystal structures of ZnS(c) and ZnS(h) were examined after the CO oxidation reaction. The two samples showed the same XRD patterns that matched well with those of hexagonal (P63mc) ZnO (JCPDS 1-089-7102). The three major peaks were observed at $2\theta = 31.7^\circ$, 34.4° and 36.2° , corresponding to the (100), (002) and (101) planes, respectively. The other peaks were assigned to the corresponding planes. The samples obtained from CO oxidation over ZnS(h) and ZnS(c) were designated ZnO-h(h) and ZnO-c(h), respectively. Based on the XRD results (Figure 6) and the CO oxidation profiles (Figure 5), ZnO was formed from ZnS via $2\text{ZnS} + 3\text{O}_2 \rightarrow 2\text{ZnO} + 2\text{SO}_2$ at above 400°C . Once ZnO is formed, CO oxidation begins to occur via $\text{ZnO} + \text{CO} + 1/2\text{O}_2 \rightarrow \text{ZnO} + \text{CO}_2$. ZnS(h) showed a lower CO oxidation onset compared to ZnS(c). The lower CO oxidation onset could be attributed to the smaller size (SEM images in Figure 1 and 6) and/or more exposed sulfur (S 2p XP spectra in Figure 3) results for ZnS(h). The BET surface area of a selected ZnS(h) was examined before and after CO oxidation. The measured BET surface area of ZnS(h) was $65.8 \text{ m}^2/\text{g}$, which decreased substantially to $17.0 \text{ m}^2/\text{g}$ after CO oxidation, forming ZnO-h(h).

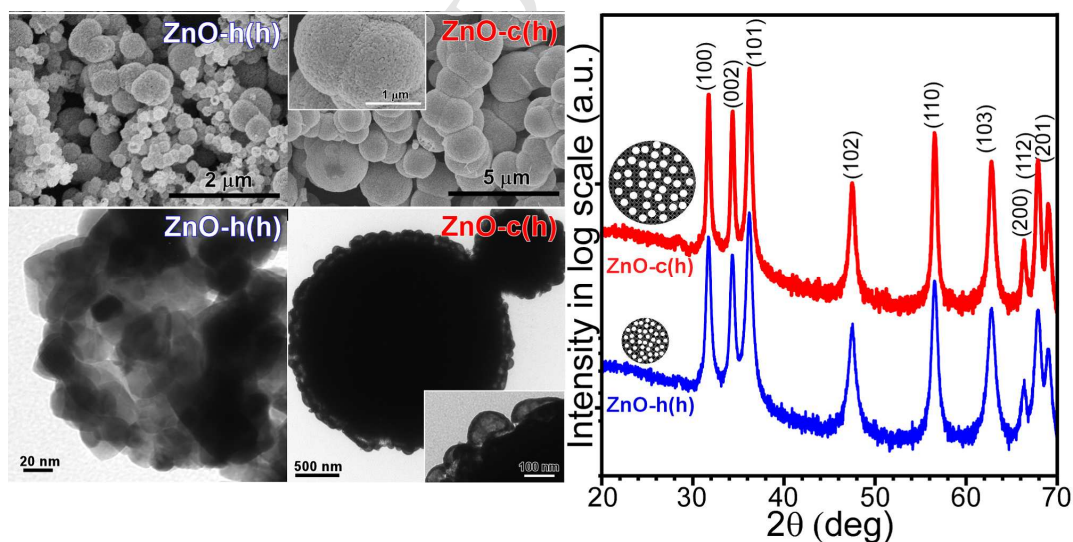


Figure 6. SEM (top left), TEM (bottom left) images and powder XRD profiles (right) of the ZnO-c(h) and ZnS-h(h) samples prepared by the CO oxidation of ZnS(c) and ZnS(h), respectively.

3.7. UV-visible absorption and PL of ZnO

Figure 7 shows UV-visible diffuse reflectance/absorption and PL spectra of the ZnO-h(h) and ZnO-c(h) samples. The reference ZnO (Sigma-Aldrich) sample showed a sharp absorption edge at approximately 387 nm (or 3.2 eV). The absorption edges of the ZnO samples extended to the visible region (red shifted) and showed smooth arising edges. Both the ZnO samples showed enhanced visible light absorption. The absorption band gaps were calculated from the plots (inset of Fig. 7) of $(\alpha h\nu)^2$ versus $h\nu$ [42,43]. The band gaps of the ZnO-h(h) and ZnO-c(h) samples were calculated to be 2.97 and 2.85 eV, respectively, which is in the visible light range.

The PL spectra of ZnO commonly showed a broad peak at 470 nm, which could be attributed to defects [2,46,51]. The PL intensity of ZnO-h(h) was somewhat lower than that of ZnO-c(h) because of high charge separation and low recombination of the charge carriers [2,46,51]. Therefore, more effective electron-hole pair separation in the ZnO-h(h) microspheres will be expected to improve the photocatalytic activity.

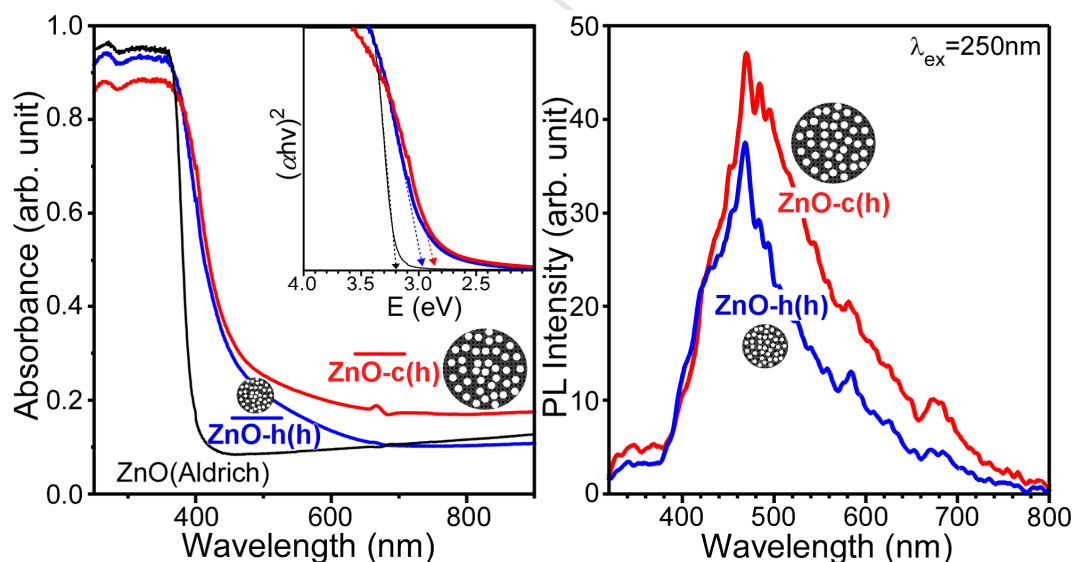


Figure 7. UV-visible diffuse reflectance/absorption (left) and PL (right) spectra of the ZnO-h(h) and ZnO-c(h) samples. The UV-Vis absorption spectrum of a commercial ZnO is shown as a reference. The excitation wavelength for PL was 250 nm.

3.8. Photocatalytic dye degradation using ZnO, ZnS(h), ZnS(c), ZnO-h(h), ZnO-c(h), Ag-ZnS(h), Ag-ZnS(c), Au-ZnS(h), and Au-ZnS(c) microspheres

The adsorption and photocatalytic performance of the ZnO-h(h) and ZnO-c(h) samples were examined for the mixed dyes. Figure 8 shows the UV-Vis absorption spectra of the two samples after adsorption in the dark and under increasing photoirradiation times. Similar to the ZnS samples, the adsorption performances of ZnO-h(h) and ZnO-c(h) were quite low. The UV-Vis absorption intensities were decreased by less than 10% (or $C_{ad}/C_0 = 90\%$). Upon irradiating with visible light for 1 hr, the UV-Vis absorption for MO was decreased abruptly, whereas that for RhB showed a negligible change. The UV-Vis absorption for MB was decreased by 15% (or $C_{1h}/C_{ad} = 85\%$) and 18% (or $C_{6h}/C_{ad} = 82\%$), where C_{1h} and C_{ad} are the UV-Vis absorption intensities after 1 hr photoirradiation and adsorption, respectively. With increasing irradiation time, the UV-Vis absorption intensities for RhB and MB decreased gradually. For MB, the UV-Vis absorption intensity decreased more rapidly than that for RhB. The photocatalytic performance over the ZnO-h(h) and ZnO-c(h) samples was in the order, RhB < MB << MO. After photoirradiation over ZnO-h(h) for 6 hrs, the UV-Vis absorption intensities for RhB and MB decreased by 61% (or $C_{6h}/C_{ad} = 39\%$) and 83% (or $C_{6h}/C_{ad} = 17\%$), respectively. For ZnO-c(h), the UV-Vis absorption intensities of RhB and MB were decreased by 51% (or $C_{6h}/C_{ad} = 49\%$) and 86% (or $C_{6h}/C_{ad} = 14\%$), respectively. In the UV-Vis absorption spectra with increasing irradiation time, no change in peak position was observed, but the peak intensity decreased gradually. This suggests that the dye molecules were oxidized/decomposed completely without forming any intermediate. The de-ethylation products from RhB were reported to be produced from active $\cdot O_2^-$ radical species [42,49,50]. As a result, the UV-Vis absorption peak of RhB is found to be blue-shifted [42,49,50]. In the present study, however, no change in peak position was observed. Therefore, $\cdot O_2^-$ radicals are not the major active species for dye degradation.

Figure 8 shows the plots of photocatalytic degradation (C_{6h}/C_{ad}) of RhB and MB in the mixed dye solution over the ZnS(h), ZnS(c), ZnO-h(h), ZnO-c(h), Ag-ZnS(h), Ag-ZnS(c), Au-ZnS(h), and Au-ZnS(c) microspheres after visible light irradiation for 6 hrs. For RhB and MB in the mixed dye, the photocatalytic activity was observed in the order,

$\text{Au-ZnS} \approx \text{Ag-ZnS} \ll \text{ZnS} < \text{ZnO}$. The undoped ZnS(c) and ZnS(h) (and Ag-doped samples) showed no critical differences in activity for both RhB and MB. On the other hand, ZnO-h(h) showed somewhat higher activity than ZnO-c(h) for RhB, but lower activity for MB. The Au-ZnS(c) showed higher activity than Au-ZnS(h) for both RhB and MB.

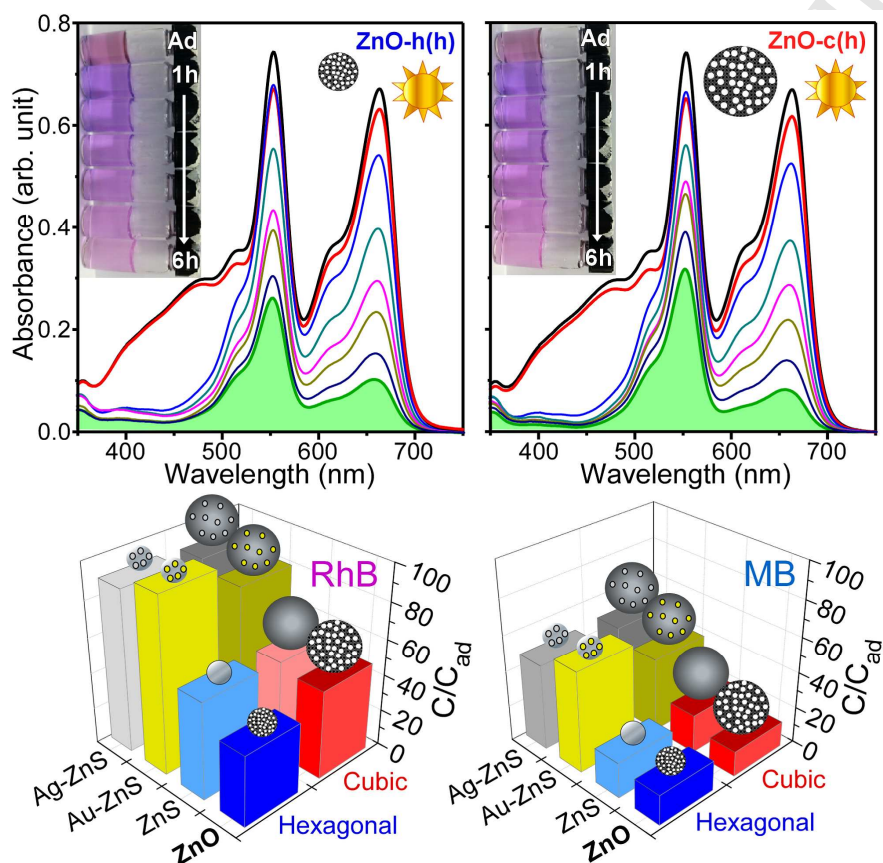


Figure 8. UV-Vis absorption spectra for the photocatalytic dye degradation (top panel) of mixed dyes under visible light over the ZnO-h(h) and ZnO-c(h) samples obtained by CO oxidation. The inset shows the corresponding degraded dye solutions. Photocatalytic degradation (C_{6h}/C_{ad}) of RhB (left) and MB (right) regions for the mixed dye solution over ZnS(h), ZnS(c), ZnO-h(h), ZnO-c(h), Ag-ZnS(h), Ag-ZnS(c), Au-ZnS(h), and Au-ZnS(c) microspheres after visible light irradiation for 6 h. C_{6h} and C_{ad} are the UV-Vis absorption intensities after 6 hrs visible irradiation and adsorption in dark, respectively.

3.9. Synthesis of 2-hydroxyterephthalic acid

Finally, this study examined the photocatalytic activity of ZnS(c), ZnS(h), ZnS-c(h), and ZnS-h(h) microspheres by probing the hydroxyl radical ($\cdot\text{OH}$) formation. For this, 2-hydroxyterephthalic acid (HTPA) synthesis was performed, which is formed by a reaction of terephthalic acid (TPA) with $\cdot\text{OH}$ radicals [41-44]. TPA is non-luminescent, whereas HTPA is luminescent, showing a broad PL band at 425 nm under the excitation of UV light. For this reason, the PL intensity is related directly to the amount of HTPA formed (or $\cdot\text{OH}$ radicals) [41-44]. Figure 9 shows the PL spectra of the TPA solutions reacted with ZnS(c), ZnS(h), ZnS-c(h), and ZnS-h(h) microspheres under visible light irradiation for 6 hrs. A broad peak was commonly observed at 425 nm, which was assigned to HTPA synthesized from TPA. The PL intensity was observed in the order, ZnS(h) < ZnS(c) << ZnO-h(h) < ZnO-c(h). ZnO showed a significantly stronger PL intensity than ZnS. The Ag and Au-doped ZnS samples also showed weak PL intensities. In addition, the larger microspheres (related with cubic phase) commonly showed a somewhat stronger PL intensity than smaller microspheres (related to hexagonal phase). This might be due to the lower band gap of ZnO-c(h) (or more absorption of visible light).

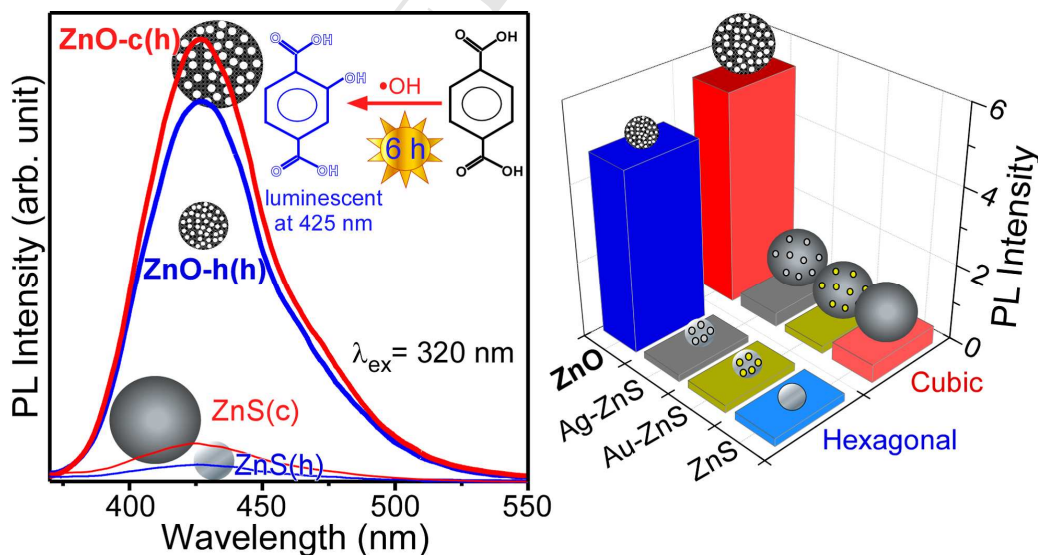
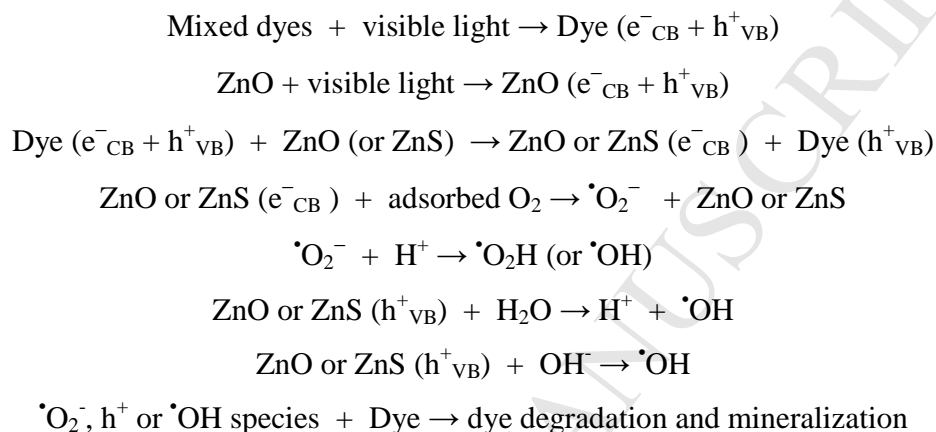


Figure 9. PL spectra (left) of the TPA solutions reacted with ZnS(c), Zn(h), ZnS-c(h), and ZnS-h(h) microspheres under visible light for 6 h. An excitation wavelength of 320 nm was used to collect the PL. PL intensities at 425 nm for ZnS(c), ZnS(h), ZnO-c(h),

ZnO-h(h), Ag/ZnS-c(h), Ag/ZnS-h(h), Au/ZnS-c(h), and Au/ZnS-h(h) microspheres. The left inset shows that terephthalic acid reacts with $\cdot\text{OH}$ to form luminescent 2-hydroxyterephthalic acid.

Based on the present photocatalytic dye degradation experiments, the following simplified mechanism can be proposed [41-44,49,50]:



Compared to ZnO (or ZnS), the dyes absorb more visible light due to conjugation. Therefore, the initial dye degradation mechanism is started mainly by formation of a hole in the valence band (VB) and an electron in the conduction band (CB) of a dye. The electrons in the CB are transferred to the CB of ZnO (or ZnS). The electron transfer efficiency is determined mainly by the aligned energy level [14,42,43]. ZnO could directly absorb visible light. This is because the calculated band gap (2.85 eV) of ZnO-c(h) is lower than that (2.97 eV) of ZnO-h(h) and ZnO-c(h), which absorbs more visible light to form electrons and holes. The active $\cdot\text{O}_2^-$ species are formed by electron capture by adsorbed oxygen, which depends on the oxygen dissolved in solution. On the other hand, based on the present study, $\cdot\text{O}_2^-$ is not a major species. Active $\cdot\text{OH}$ radicals are formed by the mechanisms described above. The formation of $\cdot\text{OH}$ radicals was much greater for ZnO than for ZnS. Therefore, mineralization/degradation of the dyes is facilitated mainly by the formation of h^+ and $\cdot\text{OH}$ species.

4. Summary

This paper reported the synthesis of different crystal phases (cubic and hexagonal) and sizes (1-3 μm and 200-300 nm) of ZnS, Ag-ZnS, and Au-ZnS microspheres, which were synthesized using a solvothermal method. Hexagonal ZnO microspheres were synthesized by a CO oxidation reaction of ZnS. The physicochemical properties of the synthesized materials were examined by UV-visible absorption/reflectance spectroscopy, PL spectroscopy, SEM, TEM/HRTEM, and XPS spectroscopy. Their photocatalytic activities and characteristics were first tested by degrading a mixed dye (MO + MB + RhB) under visible light irradiation. The dye degradation rate of the mixed dye over the photocatalysts was observed in the order, RhB < MB \ll MO, whereas the photocatalytic activity was in the order, Au-ZnS \approx Ag-ZnS \ll ZnS < ZnO. The slight photo-degraded MO was sensitized by the dyes, resulting in rapid degradation. Finally, ZnS and ZnO were also used for the successful synthesis of 2-hydroxyterephthalic acid from terephthalic acid under visible light irradiation. ZnO showed \sim 6 times more $\bullet\text{OH}$ radical formation activity (probed from the synthesis of 2-hydroxyterephthalic acid) than the ZnS and metal-doped ZnS. The CO oxidation activity was observed at above 350°C. The activity was higher for smaller size ZnO and became lower after Au and Ag doping. This novel method can offer new strategies for the synthesis of chalcogenides (such as ZnS), metal oxides (such as ZnO), and nanocomposites (such as Ag-ZnS and Au-ZnS) for visible light-induced photocatalysis as well as a facile route to synthesis of novel chemicals.

Acknowledgements. This study was supported financially by a National Research Foundation of Korea (NRF) grant funded by the Korean government (MEST) (NRF-2014R1A1A2055923).

References

1. M. M. Khan, S. A. Ansari, D. Pradhan, M. O. Ansari, D. H. Han, J. Lee and M. H. Cho, Band gap engineered TiO_2 nanoparticles for visible light induced

- photoelectrochemical and photocatalytic studies, *J. Mater. Chem. A* 2014, 2 (2014) 637–644.
2. S. A. Ansari, M. M. Khan, S. Kalathil, A. Nisar, J. Lee and M. H. Cho, Oxygen Vacancy Induced Band Gap Narrowing of ZnO Nanostructure by Electrochemically Active Biofilm, *Nanoscale* 5 (2013) 9238–9246.
 3. S. A. Ansari, M. Mansoob Khan, M. O. Ansari, J. Lee and M. H. Cho, Highly photoactive SnO₂ nanostructures engineered by electrochemically active biofilm, *New J. Chem.* 38 (2014) 2462–2469.
 4. M. M. Khan, S. A. Ansari, D. Pradhan, D. H. Han, J. Lee and M. H. Cho, Defect-Induced Band Gap Narrowed CeO₂ Nanostructures for Visible Light Activities, *Ind. Eng. Chem. Res.* 53 (2014) 9754–9763.
 5. S. Satter, M. Hoque, M. Rahman, M. Mollah and M. Susan, An approach towards the synthesis and characterization of ZnO@Ag core@shell nanoparticles in water-in-oil microemulsion, *RSC Adv.* 4 (2014) 20612-20615.
 6. H. Barani, Surface activation of cotton fiber by seeding silver nanoparticles and in situ synthesizing ZnO nanoparticles, *New J. Chem.* 2014, 38 (2014) 4365-4370.
 7. Z. Li, F. Zhang, A. Meng, C. Xie and J. Xing, ZnO/Ag micro/nanospheres with enhanced photocatalytic and antibacterial properties synthesized by a novel continuous synthesis method, *RSC Adv.* 5 (2015) 612-620.
 8. B. Divbanda, M. Khatamiana, G. Eslamianb and M. Darbandi, Synthesis of Ag/ZnO nanostructures by different methods and investigation of their photocatalytic efficiency for 4-nitrophenol degradation, *Appl. Surf. Sci.*, 284 (2013) 80–86.
 9. S. Motshekga, S. Ray, M. Onyango and M. Momba, Microwave-assisted synthesis, characterization and antibacterial activity of Ag/ZnO nanoparticles supported bentonite clay, *J. Hazard. Mater.* 262 (2013) 439–446.
 10. Y. Zuo, Y. Qin, C. Jin, Y. Li, D. Shi, Q. Wu and J. Yang, Double-sided ZnO nanorods arrays on single-crystal Ag holed microdisks with enhanced photocatalytic efficiency, *Nanoscale* 5 (2013) 4388-4394.
 11. G. Tang, S. Tian, Z. Zhou, Y. Wen, A. Pang, Y. Zhang, D. Zeng, H. Li, B. Shan and C. Xie, ZnO Micro/Nanocrystals with Tunable Exposed (0001) Facets for Enhanced

- Catalytic Activity on the Thermal Decomposition of Ammonium Perchlorate, *J. Phys. Chem. C* 118 (2014) 11833–11841.
12. P. G. Li, W. H. Tang, X. Wang, Synthesis of ZnO nanowire arrays and their photoluminescence property, *J. Alloys Compd.* 479 (2009) 634–637.
 13. Y. Zheng, C. Chen, Y. Zhan, X. Lin, Q. Zheng, K. Wei and J. Zhu, Photocatalytic activity of Ag/ZnO heterostructure nanocatalyst: correlation between structure and property, *J. Phys. Chem. C.* 112 (2008) 10773–10777.
 14. S. Ansari, M. Khan, M. Ansari, J. Lee and M. Cho, Biogenic Synthesis, Photocatalytic, and Photoelectrochemical Performance of Ag–ZnO Nanocomposite, *J. Phys. Chem. C.* 117 (2013) 27023–2703.
 15. M. Alenezi, S. Henley, N. Emerson and S. Silva, From 1D and 2D ZnO nanostructures to 3D hierarchical structures with enhanced gas sensing properties, *Nanoscale* 6 (2014) 235–247.
 16. D. Su, H. Fu, X. Jiang and G. Wang, ZnO nanocrystals with a high percentage of exposed {42⁻2⁻3⁻} reactive facets for enhanced gas sensing performance, *Sens. Actuators. B* 186 (2013) 286–292.
 17. H. Ma, P. Williams and S. Diamond, Ecotoxicity of manufactured ZnO nanoparticles - A review, *Environ. Pollut.* 172 (2013) 76–85.
 18. J. Fang, H. Fan, Y. Ma, Z. Wang and Q. Chang, Surface defects control for ZnO nanorods synthesized by quenching and their anti-recombination in photocatalysis, *Appl. Surf. Sci.* 332 (2015) 47–54.
 19. S. Kundu, S. Sain, B. Satpati, S. Bhattacharyyab and S. Pradhan, Structural interpretation, growth mechanism and optical properties of ZnO nanorods synthesized by a simple wet chemical route, *RSC Adv.* 5 (2015) 23101–23113.
 20. D. Pradhan, Z. Su, S. Sindhwani, J. Honek and K. T. Leung, Electrochemical growth of ZnO nanobelt-like structures at 0°C: synthesis, characterization, and in-situ glucose oxidase embedment, *J. Phys. Chem. C.* 115 (2011) 18149–18156.
 21. C. Wanga, Y. Ao, P. Wang, S. Zhang, J. Qian, J. Hou, A simple method for large-scale preparation of ZnS nanoribbon film and its photocatalytic activity for dye degradation, *Appl. Surf. Sci.* 256 (2010) 4125–4128.

22. N. Soltania, E. Saiona, W. M. M. Yunusa, M. Erfania, M. Navaserya, G. Bahmanrokha, K. Rezaee, Enhancement of visible light photocatalytic activity of ZnS and CdS nanoparticles based on organic and inorganic coating, *Appl. Surf. Sci.* 290 (2014) 440–447.
23. A. L. Stroyuk, A. E. Raevskaya, A. V. Korzhak and S. Y. Kuchmii, Zinc sulfide nanoparticles: Spectral properties and photocatalytic activity in metals reduction reactions, *J. Nanopar. Res.* 9 (2007) 1027–1039.
24. X. Fang, T. Zhai, U. K. Gautam, L. Li, L. Wua, Y. Bando and D. Golberg, ZnS nanostructures: From synthesis to applications, *Prog. Mater. Sci.* 56 (2011) 175–287.
25. M. Misra, R. K. Gupta, A. K. Paul and M. Singla, Influence of gold core concentration on visible photocatalytic activity of gold-zinc sulfide core-shell nanoparticle, *J. Power Sources* 294 (2015) 580-587
26. T. Baran, S. Wojtyla, A. Dibenedetto, M. Arest and W. Macyk, Zinc sulfide functionalized with ruthenium nanoparticles for photocatalytic reduction of CO₂, *Appl. Catal. B* 178 (2015) 170–176
27. X. Xiao, X.-B. Ma, H. Yuan, P.-C. Liu, Y.-B. Lei, H. Xu, D.-L. Du, J.-F. Sun and Y.-J. Feng, Photocatalytic properties of zinc sulfide nanocrystals biofabricated by metal-reducing bacterium *Shewanella oneidensis* MR-1, *J. Hazard. Mater.* 288 (2015) 134–139
28. A. Roychowdhury, S. P. Pati, S. Kumar and D. Das, Effects of magnetite nanoparticles on optical properties of zinc sulfide in fluorescent-magnetic Fe₃O₄/ZnS nanocomposites, *Powder Technol.* 254 (2014) 583–590.
29. D. Zhu, W. Li, H.-M. Wen, Y. Hu, J. Wang, J.-M. Zhu, W.-T. Ni and C.-Q. Gu, Development of polyacrylic acid-functionalized porous zinc sulfide nanospheres for a non-aqueous solid phase extraction procedure toward alkaloids, *RSC Adv.* 5 (2015) 29820–29827.
30. S. K. Dash, T. Ghosh, S. Roy, S. Chattopadhyay and D. Das, Zinc sulfide nanoparticles selectively induce cytotoxic and genotoxic effects on leukemic cells: involvement of reactive oxygen species and tumor necrosis factor alpha, *J. Appl. Toxicol.* 34 (2014) 1130-1144.

31. T. Baran, A. Dibenedetto, M. Aresta, K. Kruczala and W. Macyk, Photocatalytic Carboxylation of Organic Substrates with Carbon Dioxide at Zinc Sulfide with Deposited Ruthenium Nanoparticles, *ChemPlusChem* 79 (2014) 708-715.
32. E. Baniyadi, I. Dincer and G. F. Naterer, Hybrid photocatalytic water splitting for an expanded range of the solar spectrum with cadmium sulfide and zinc sulfide catalysts, *Appl. Catal. A* 455 (2013) 25-32.
33. X. Zeng, S. S. Pramana, S. K. Batabyal, S. G. Mhaisalkar, X. Chen and K. B. Jinesh, Low temperature synthesis of wurtzite zinc sulfide(ZnS) thin films by chemical spray pyrolysis, *Phys. Chem. Chem. Phys.* 15 (2013) 6763-6768
34. E. Baniyadi, I. Dincer and G. F. Naterer, Measured effects of light intensity and catalyst concentration on photocatalytic hydrogen and oxygen production with zinc sulfide suspensions, *Int. J. Hydrogen Energy* 38 (2013) 9158-9168.
35. J. Manna, S. Goswami, N. Shilpa, N. Sahu, and R. K. Rana, Biomimetic Method To Assemble Nanostructured Ag@ZnO on Cotton Fabrics: Application as Self-Cleaning Flexible Materials with Visible-Light Photocatalysis and Antibacterial Activities, *ACS Appl. Mater. Interfaces* 7 (2015) 8076–8082.
36. M. Height, S. Pratsinis, O. Mekasuwandumrong and P. Praserthdam, Ag-ZnO catalysts for UV-photodegradation of methylene blue, *Appl. Catal. B* 63 (2006) 305-312.
37. M. Khan, C. Wei, M. Chen, J. Tao, N. Huang, Z. Qi and L. Li, CTAB-mediated synthesis and characterization of ZnO/Ag core-shell nanocomposites, *J. Alloys Compd.* 612 (2014) 306–314.
38. Y. Zang, J. Yin, X. He, C. Yue, Z. Wu, J. Li and J. Kang, Plasmonic-enhanced self-cleaning activity on asymmetric Ag/ZnO surface-enhanced Raman scattering substrates under UV and visible light irradiation, *J. Mater. Chem. A* 2 (2014) 7747-7753.
39. S. Ansari, M. Khan, J. Lee and M. Cho, Highly visible light active Ag@ZnO nanocomposites synthesized by gel-combustion route, *J. Ind. Eng. Chem.* 20 (2014) 1602-1607.

40. M. Hsu and C. Chang, Ag-doped ZnO nanorods coated metal wire meshes as hierarchical photocatalysts with high visible-light driven photoactivity and photostability, *J. Hazard. Mater.* 278 (2014) 444–453.
41. Y. I. Choi, H. J. Jung, W. G. Shin and Y. Sohn, Band gap-engineered ZnO and Ag/ZnO by ball-milling method and their photocatalytic and Fenton-like photocatalytic activities, *Appl. Surf. Sci.* 356 (2015) 615–625.
42. Y. Park, Y. Na, D. Pradhan, B. Min and Y. Sohn, Adsorption and UV/Visible photocatalytic performance of BiOI for methyl orange, Rhodamine B and methylene blue: Ag and Ti-loading effects, *CrystEngComm* 16 (2014) 3155–3167.
43. W. Kim, D. Pradhan, B. Min and Y. Sohn, Adsorption/photocatalytic activity and fundamental natures of BiOCl and BiOCl_xI_{1-x} prepared in water and ethylene glycol environments, and Ag and Au-doping effects, *Appl. Catal. B.* 147 (2014) 711–725.
44. Y. Na, Y. Kim, D. Cho, D. Pradhan and Y. Sohn, Adsorption/photocatalytic performances of hierarchical flowerlike BiOBr_xCl_{1-x} nanostructures for methyl orange, Rhodamine B and methylene blue, *Mater. Sci. Semicond. Process.* 27 (2014) 181–190.
45. A. Nayak, S. Lee, Y. Sohn and D. Pradhan, Synthesis of In₂S₃ microspheres using a template-free and surfactant-less hydrothermal process and their visible light photocatalysis, *CrystEngComm* 16 (2014) 8064–8072.
46. G. Wang, B. Huang, Z. Li, Z. Lou, Z. Wang, Y. Dai and M.-H. Whangbo, Synthesis and characterization of ZnS with controlled amount of S vacancies for photocatalytic H₂ production under visible light, *Sci. Rep.* 5 (2015) 8544.
47. L. Yu, W. Chen, D. Li, J. Wang, Y. Shao, M. He, P. Wang and X. Zheng, Inhibition of photocorrosion and photoactivity enhancement for ZnO via specific hollow ZnO core/ZnS shell structure, *Appl. Catal. B* 164 (2015) 453–461.
48. Y. -P. Zhu, J. Li, T. -Y. Ma, Y. -P. Liu, G. Du and Z. -Y. Yuan, Sonochemistry-assisted synthesis and optical properties of mesoporous ZnS nanomaterials, *J. Mater. Chem. A* 2 (2014) 1093–1101.
49. Y. I. Choi, Y. I. Kim, D. W. Cho, J. S. Kang, K. T. Leung and Y. Sohn, Recyclable magnetic CoFe₂O₄/BiOX (X= Cl, Br and I) microflowers for photocatalytic treatment

- of water contaminated with methyl orange, rhodamine B, methylene blue, and a mixed dye, *RSC Adv.* 5 (2015) 79624-79634.
50. H. J. Yoon, Y. I. Choi, E. S. Jang and Y. Sohn, Graphene, charcoal, ZnO, and ZnS/BiOX (X= Cl, Br, and I) hybrid microspheres for photocatalytic simulated real mixed dye treatments, *J. Ind. Eng. Chem.* 32 (2015) 137-152.
51. W. Kim, D. Pradhan and Y. Sohn, Fundamental nature and CO oxidation activities of indium oxide nanostructures: 1D-wires, 2D-plates, and 3D-cubes and donuts, *J. Mater. Chem. A*, 2013, 1, 10193-10202.
52. W. Kim, S. Lee and Y. Sohn, Metallic Sn spheres and SnO₂@C core-shells by anaerobic and aerobic catalytic ethanol and CO oxidation reactions over SnO₂ nanoparticles, *Sci. Rep.* 5 (2015) 13448.
53. Y. Park, S. Kim, D. Pradhan and Y. Sohn, Surface treatment effects on CO oxidation reactions over Co, Cu, and Ni-doped and codoped CeO₂ catalysts, *Chem. Eng. J.* 250 (2014) 25-34.
54. S. Lee, S. Park, B. Min, J. Kang and Y. Sohn, Structural/spectroscopic analyses and H₂/O₂/CO responses of thulium (III) oxide nanosquare sheets, *Appl. Surf. Sci.* 307 (2014) 736-743.
55. Y. Na, S.W. Lee, N. Roy, D. Pradhan and Y. Sohn, Room temperature light-induced recrystallization of Cu₂O cubes to CuO nanostructures in water, *CrystEngComm* 16 (2014) 8546-8554.
56. Y. Sohn, SiO₂ nanospheres modified by Ag nanoparticles: Surface charging and CO oxidation activity, *J. Mol. Catal. A.* 379 (2013) 59-67.
57. Y. Park, S. Kim, D. Pradhan and Y. Sohn, Thermal H₂-treatment effects on CO/CO₂ conversion over Pd-doped CeO₂ comparison with Au and Ag-doped CeO₂, *React. Kinet. Mech.Catal.* 113 (2014) 85-100.

Highlights

- ▶ Undoped, Au and Ag-doped cubic and hexagonal ZnS microspheres were prepared.
- ▶ Hexagonal ZnO microspheres were prepared by post-CO oxidation of the ZnS.
- ▶ Photocatalytic dye degradation was tested for mixed dye (MO + RhB + MB) under visible light.
- ▶ Photocatalytic synthesis of 2-hydroxyterephthalic acid was examined.